Characteristics of the Marine Atmospheric Boundary Layer under the Influence of Ocean Surface Waves

CHANGLONG LIU,[a] XINYU LI,[a] JINBAO SONG,[a] ZHONGSHUI ZOU,[a,b] JIAN HUANG,[c] JUN A. ZHANG,[d,e] GANXIN JIE,[f] AND JUN WANG[f]

[a] *Ocean College, Zhejiang University, Zhoushan, China*
[b] *School of Marine Science, Sun Yat-Sen University, Zhuhai, China*
[c] *Guangzhou Institute of Tropical and Marine Meteorology, CMA, Guangdong, China*
[d] *Cooperative Institute for Marine and Atmospheric Studies, University of Miami, Miami, Florida*
[e] *Hurricane Research Division, NOAA/AOML, Miami, Florida*
[f] *State Key Laboratory of Environmental Adaptability for Industrial Products, China National Electric Apparatus Research Institute Co., Ltd., Guangzhou, China*

(Manuscript received 30 July 2021, in final form 26 February 2022)

ABSTRACT: The deviation of the mean wind profile from Monin–Obukhov similarity theory (MOST) within the wave boundary layer (WBL) is investigated by combining four levels of turbulence data measured on a fixed platform with wave measurements. The data suggest that the mean wind profile follows MOST under wind-sea conditions because the turbulence statistics and structure are consistent with the attached eddy model. However, pronounced swell-related peaks appeared in the velocity spectra and *uw* cospectra under swell conditions. The upward wave-induced stress resulted in a large wind gradient within the WBL when light winds traveled with the swell, while the opposite result was found for the wind-opposite swell. These phenomena were analyzed based on the velocity spectra and turbulence variances. We found that the deviation of the wind profile was due to the longer or shorter length of the f^{-1} scaling region appearing in the velocity spectra.

SIGNIFICANCE STATEMENT: The interactions between ocean waves and adjacent airflow affect the functioning of Earth's climate and weather systems. However, our physical understanding of air–wave interactions remains incomplete, for example, the deviation of the mean wind profile from Monin–Obukhov similarity theory within the wave boundary layer. In this study, we aim to provide new insights by analyzing four-level turbulence data and wave measurements. We found that when the local wind travels faster than the wave, the airflow over the wavy surface is similar to that over land because the effects of waves do not reach the measurement heights. In conditions with wind-following or -opposing fast-propagating waves, the overlying airflow is greatly modified as the turbulence is affected by wave-induced perturbations.

KEYWORDS: Air–sea interaction; Boundary layer; Oceanic waves; Turbulence; Wind stress

1. Introduction

Atmospheric boundary layer (ABL) turbulence over the ocean surface is typically assumed to be similar to that over a flat rigid surface, but it has its own unique features due to the influence of surface waves. Unlike the turbulence generated by wind shear and buoyancy force, the fluctuations over ocean surface waves also include wave-induced (-coherent) perturbations, which leads to distinct features of the mean wind profile and momentum exchanges between the atmosphere and the ocean. Thus, a comprehensive understanding of wave-modulated turbulence can elucidate these unique features and help to make accurate predictions in the marine ABL (MABL; Yousefi et al. 2020).

a. Turbulent flow over a flat rigid surface

Wall-bounded turbulence has been extensively studied in the laboratory based on Townsend's attached eddy hypothesis (Townsend 1976) and the attached eddy model (AEM; Perry and Chong 1982; Perry et al. 1986; Perry and Marusic 1995; Marusic and Perry 1995) because these theories can provide accurate predictions of the scaling behaviors for various turbulence statistics (Marusic and Monty 2019). The AEM is also ideally suited for describing very-high-Reynolds-number atmospheric-surface-layer flows (e.g., Hutchins et al. 2012).

Townsend (1976) proposed that the logarithmic profile of the mean velocity U is associated with energy-containing attached eddies, whose sizes scale with the distance from the surface z, and with population densities varying inversely with their sizes. This hypothesis leads to a logarithmic profile for the horizontal turbulence intensities, which is similar to the logarithmic profile of U. Perry and Chong (1982) extended this hypothesis into a model by introducing a Λ-shaped vortex (or hairpin vortex) and showed that the logarithmic profiles of the mean velocity and the horizontal turbulence intensities can hold simultaneously which has been supported by boundary layer and atmospheric surface-layer data over the past decade (e.g., Marusic et al. 2013).

Supplemental information related to this paper is available at the Journals Online website: https://doi.org/10.1175/JPO-D-21-0164.s1.

Corresponding author: Zhongshui Zou, zouzhsh3@mail.sysu.edu.cn

DOI: 10.1175/JPO-D-21-0164.1

The AEM predicts that in addition to the −5/3 power-law region (inertial subrange) at the high-wavenumber range of the velocity spectra, a k^{-1} scaling region also exists at low wavenumbers near the −5/3 power law in the horizontal velocity spectra, while the −1 power law is absent in the vertical velocity spectra. The −1 power-law region represents eddies that transfer fluxes more efficiently than others (Li et al. 2018) and has been validated by numerous experiments (e.g., Katul and Chu 1998; Kunkel and Marusic 2006; del Álamo and Jiménez 2009; Katul et al. 2012). These studies showed that the horizontal velocity spectra in the near-neutral ABL follow the AEM.

However, the results of the vertical velocity spectra are at times contradictory. For example, Ghannam et al. (2018) reported results from three experiments that showed a −1 power-law region in the vertical spectra and two experiments that did not. The controversy regarding the vertical spectra is also reflected in rapid distortion theory (Hunt and Carlotti 2001) and the dimensional analysis of Kader and Yaglom (1991) and Yaglom (1991).

To explain the mixed findings of the vertical velocity spectra, Drobinski et al. (2004) suggested that the near-neutral atmospheric surface layer can be divided into at least two sublayers. The first is the lower sublayer where the blocking of impinging eddies is the dominating mechanism (the eddy surface layer), so the vertical velocity spectra S_{ww} are independent of frequency f at the intermediate-frequency range. The second is far from the surface where the sublayer is dominated by the shear (the shear surface layer) and S_{ww} follows the prediction of Yaglom (1991), i.e., a −1 power-law region is expected.

In summary, based on the above studies, the universal scaling shape of the velocity spectra is given by (Nikora 1999; Högström et al. 2002; Drobinski et al. 2004; Banerjee and Katul 2013):

$$S_{uu}(k) \propto \begin{cases} k^{-5/3}, & k > a_1 z^{-1} \\ k^{-1}, & a_2 H^{-1} < k < a_1 z^{-1} \\ k^{0}, & k < a_2 H^{-1} \end{cases},$$

$$S_{ww}(k) \propto \begin{cases} k^{-5/3}, & k > b_1 z^{-1} \\ k^{-1}, & b_2 H^{-1} < k < b_1 z^{-1} \\ k^{0}, & k < b_2 H^{-1} \end{cases}, \quad (1)$$

or in frequency form:

$$S_{uu}(f) \propto \begin{cases} f^{-5/3}, & f > a_1 U/(2\pi z) \\ f^{-1}, & a_2 U/(2\pi H) < f < a_1 U/(2\pi z) \\ f^{0}, & f < a_2 U/(2\pi H) \end{cases},$$

$$S_{ww}(f) \propto \begin{cases} f^{-5/3}, & f > b_1 U/(2\pi z) \\ f^{-1}, & b_2 U/(2\pi H) < f < b_1 U/(2\pi z) \\ f^{0}, & f < b_2 U/(2\pi H) \end{cases}, \quad (2)$$

considering the influence of the very large-scale motion (Guala et al. 2006; Balakumar and Adrian 2007). Here, a_1, a_2, b_1, and b_2 are constant depending on the terrain characteristic; the wavenumber k and frequency f are related by Taylor's hypothesis ($k = 2\pi f/U$); and $H \sim \delta$ is the external length scale of the flow, where δ is the boundary layer thickness. For the lateral velocity spectra S_{vv}, it is often assumed that they have a similar scaling shape as S_{uu}. The vertical spectra contain k^{-1} or f^{-1} scaling only within the shear surface layer.

The −1 law is of particular interest because it represents the production range of turbulence and corresponds to the main energy-containing eddies. By integrating the horizontal spectra [Eq. (2)] over the frequency range where the −1 and −5/3 laws hold, we obtain

$$\overline{u'^2}/u_*^2 = B_1 - A_1 \ln(z/\delta), \quad \overline{v'^2}/u_*^2 = B_2 - A_2 \ln(z/\delta). \quad (3)$$

Hence, the −1 power law and Eq. (3) are equivalent. Equation (3) also shows that, as with the logarithmic profile of the mean velocity, the horizontal turbulence variances follow a logarithmic law. However, formats of the vertical and horizontal turbulence variances differ due to their various spectral shapes. According to the AEM or the rapid distortion theory, it is

$$\overline{w'^2}/u_*^2 = B_3 \quad (4a)$$

or

$$\overline{w'^2}/u_*^2 = B_4 + A_3(z)^{2/3}. \quad (4b)$$

Here, the overbar in Eqs. (3) and (4) signifies the ensemble average; u', v', and w' are the longitudinal (streamwise), lateral (spanwise) and vertical (wall-normal) turbulent fluctuations, respectively; $u_* = \sqrt{\rho^{-1}|\boldsymbol{\tau}_t|}$ is the friction velocity, where $\boldsymbol{\tau}_t$ is turbulent stress; ρ is the density of the fluid; and A_1, A_2, A_3, B_1, B_2, B_3, and B_4 are constants.

b. Marine atmospheric boundary layer

Within the MABL, the total wind stress $\boldsymbol{\tau}$ is (e.g., Drennan et al. 1999; Grachev et al. 2003):

$$\boldsymbol{\tau} = \boldsymbol{\tau}_x + \boldsymbol{\tau}_y = (-\rho\overline{uw})\mathbf{i} + (-\rho\overline{vw})\mathbf{j}, \quad (5)$$

where $\mathbf{i}$ and $\mathbf{j}$ represent the longitudinal (along-wind) and lateral (crosswind) unit vectors; u, v, and w are the fluctuations of the longitudinal, lateral, and vertical velocity components around their time-averaged values, respectively; and ρ is the air density. The magnitude of $\boldsymbol{\tau}$ is numerically equal to $|\tau|$, where τ is the vertical momentum flux and is defined to be positive downward (from atmosphere to ocean), so we do not differentiate between stress and momentum flux in the literal description. It is a common practice to take along-wind stress $\boldsymbol{\tau}_x$ as the total wind stress, because crosswind stress $\boldsymbol{\tau}_y$ is too small to change the magnitude and direction of the total wind stress. However, under swell conditions, studies (Grachev et al. 2003; Chen et al. 2019) have shown that swell cannot only lead along-wind stress to reverse its sign but can also cause a substantial portion of crosswind stress, resulting in a misalignment between the stress vector and the wind.

The wave boundary layer (WBL) is defined as the region of the MABL directly impacted by waves. Over wind seas, the WBL is thin and lies below typical measurement heights (Makin and Kudryavtsev 1999; Drennan et al. 1999) but can

extend to tens of meters or even the whole surface layer when the swell is present (Rutgersson et al. 2001; Semedo et al. 2009; Chen et al. 2019). Within the WBL, but above the viscous sublayer, the fluctuations of wind velocity can be divided into turbulent and wave-induced fluctuations, e.g., $u = u' + \tilde{u}$, where primes denote turbulent fluctuations and tildes represent wave-induced fluctuations (e.g., Hare et al. 1997; Buckley and Veron 2016). Thus, the total wind stress is the sum of turbulent stress $\boldsymbol{\tau}_t$ and wave-induced stress $\boldsymbol{\tau}_w$ (Phillips 1977): $\boldsymbol{\tau} = \boldsymbol{\tau}_t + \boldsymbol{\tau}_w$, where

$$\begin{aligned} \boldsymbol{\tau}_t &= -\rho\overline{u'w'}\mathbf{i} - \rho\overline{v'w'}\mathbf{j}, \\ \boldsymbol{\tau}_w &= -\rho\overline{\tilde{u}\tilde{w}}\mathbf{i} - \rho\overline{\tilde{v}\tilde{w}}\mathbf{j}, \end{aligned} \tag{6}$$

or in the format of cospectra:

$$\begin{aligned} \boldsymbol{\tau} &= -\int_0^{+\infty} \rho \mathrm{Co}_{uw}(f)df\mathbf{i} - \int_0^{+\infty} \rho \mathrm{Co}_{vw}(f)df\mathbf{j}, \\ \boldsymbol{\tau}_t &= -\int_0^{+\infty} \rho \mathrm{Co}_{u'w'}(f)df\mathbf{i} - \int_0^{+\infty} \rho \mathrm{Co}_{v'w'}(f)df\mathbf{j}, \\ \boldsymbol{\tau}_w &= -\int_0^{+\infty} \rho \mathrm{Co}_{\tilde{u}\tilde{w}}(f)df\mathbf{i} - \int_0^{+\infty} \rho \mathrm{Co}_{\tilde{v}\tilde{w}}(f)df\mathbf{j}, \end{aligned} \tag{7}$$

where Co is the cospectra.

The wave-induced momentum flux τ_w can be positive or negative, depending on the wave age and the relative angle between the wind stress and dominant wave (Zou et al. 2019). Young wind waves extract momentum from the wind (Grare et al. 2013; Kahma et al. 2016), but for the swell that travels faster than the local wind, the upward momentum flux occurs when the swell travels along with the local wind (Grachev and Fairall 2001; Sullivan et al. 2008; Kahma et al. 2016), whereas the swell absorbs energy from the wind in situations with it traveling against the wind (e.g., Donelan et al. 1997; Zou et al. 2019).

c. *Objectives of this study*

Over the ocean surface, Monin–Obukhov similarity theory (MOST; Monin and Obukhov 1954), which was developed from the rigid land surface, is widely used to relate the wind stress to the mean wind profile based on the logarithmic velocity profile:

$$U/u_* = \kappa^{-1}[\ln(z/z_0) - \psi_m(z/L)]. \tag{8}$$

Here, κ is the dimensionless von Kármán constant; z_0 is the roughness length; ψ_m is the stability function; and z/L is the atmospheric stability parameter, where L is the Obukhov length:

$$L = \frac{-\overline{T}_v u_*^3}{\kappa g \overline{w'T_v'}}, \tag{9}$$

where T_v is the virtual potential temperature, and g is the gravitational acceleration. Under neutral atmospheric stratification, the logarithmic mean velocity profile

$$U/u_* = \kappa^{-1}\ln(z/z_0) \tag{10}$$

can be obtained, and Eqs. (3) and (10) both depict the eddies that transfer momentum more efficiently than other eddies.

Many studies (e.g., Hanley and Belcher 2008; Wu et al. 2016; Song et al. 2015) have shown that under swell conditions, the shape of the wind profile deviates from MOST when swell waves exert upward momentum, indicating the invalidity of MOST within the MABL. To our knowledge, this is the first time the wind profile has been analyzed for cases when swell waves extract momentum from the MABL. To interpret the discrepancy between the eddy covariance method and inertial dissipation method, a recent study by Zou et al. (2020) suggested that MOST only depicts the wind-shear- and buoyancy-generated turbulence. However, they only give the intuitive reflection of swell wave's effect rather than its essence. Therefore, the question of how the turbulence characteristics react under the modulation of the surface wave is still unanswered.

Considering that the −1 power law in the velocity spectra is equivalent to the logarithmic variation of the turbulence variances [Eqs. (1)–(3)] and that the logarithmic profile of the mean velocity and the horizontal turbulence intensities hold simultaneously [Eqs. (3) and (10)], the deviation of the wind profile from MOST within the MABL may be due to its distinct turbulence features. Another question is whether the wind profile follows a logarithmic law above the WBL and, if so, does it mean that the turbulence above the WBL is immune to the wave effect?

To answer these questions, we used the AEM to analyze the characteristics of the MABL (i.e., the wind profile, velocity spectra and cospectra) based on four-level turbulence data measured at a stable platform combined with wave measurements. In section 2, we describe field observations and the selection of data. The results are presented in section 3 and the analysis of the results is presented in section 4. The discussion and conclusions are provided in sections 5 and 6, respectively.

2. Data

The field observations used in this study were collected in the northern South China Sea from 19 February to 8 May 2012. The observation site, 21°26.5′N, 111°23.5′E (Fig. 1a), surrounded by ~16-m-deep water, is ~6.5 km away from the coastline. Meteorological and surface wave data were measured simultaneously to assess air–sea interactions. A 53-m-tall tower (Fig. 1b) served as a platform to mount meteorological instruments, including four sets of Gill R3-50 ultrasonic anemometers at fixed heights of 8, 20, 28, and 36 m above the mean ocean level to sample three components of velocity at 20 Hz. An open-path CO_2/H_2O analyzer (LI-COR 7500) and an ultrasonic anemometer (Campbell CSAT3) were used to measure water vapor concentrations, sonic temperature, and wind velocity at 20 m with a sampling frequency of 10 Hz to calculate the flux of the virtual potential temperature. An acoustic wave and current (AWAC) sensor (Nortek, Rud, Norway) was used to measure directional wave data at 1 Hz, and the horizontal distance between the AWAC and the tower was ~100 m. More details of the experiment can be found in Zou et al. (2017) and Zou et al. (2019).

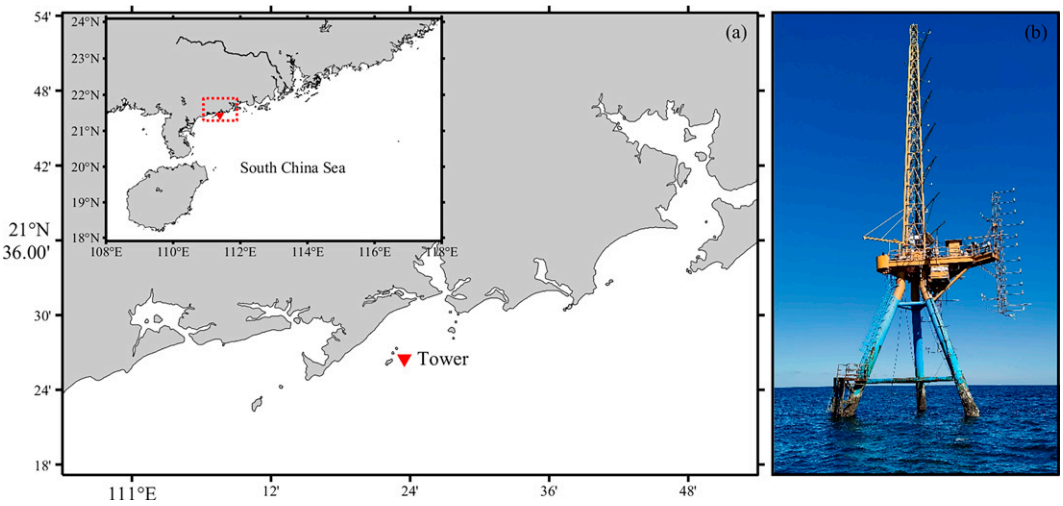

FIG. 1. (a) Location of the observation site (21°26.5′N, 111°23.5′E) and (b) photograph of the observation tower. Red triangles denote the observation tower.

Due to the complexity of environmental conditions, strict quality control procedures should be applied to field observations to guarantee the accuracy of the results, including spike removal, tilt correction, and mesoscale motion removal (Zou et al. 2017). After applying the quality control procedures, 444 runs were obtained. The evolution of the main meteorological and surface wave parameters of these runs are plotted in Fig. 2 to provide a general overview of the environmental conditions, which is similar to Grachev et al. (2018). The mean values and fluxes were computed over 30-min records. The x axis represents the date in days during 2012, using the coordinated universal time (UTC).

Figure 2a shows the mean wind speed at 8 m U_8 and the wave age c_p/U_8. Here, $c_p = g/\omega_p \tanh(\omega_p h/c_p)$ is the phase speed at the peak of the wave elevation spectra (Smedman et al. 2003), where h is the water depth and ω_p is the peak wave frequency. The wave age was calculated by the measured U_8 instead of the standard 10-m wind speed, as MOST is questionable when swell is present (Drennan et al. 2003). The wind speed ranged between 2 and 9 m s^{-1} except for in approximately 20 runs with wind speed of less than 2 m s^{-1} and 20 runs with wind speed of greater than 9 m s^{-1}. The wave age was between 0.8 and 4 except for ~40 runs with very small or large wave age.

Figure 2b shows the wind direction and the direction of the dominant waves (both "from" direction, 0° is north and 90° is east). The wind direction had a wide range, from 0° to 210°, and in 40% of the runs, the wind direction was between 70° and 100°. The main direction of the waves, however, remained quite steady, as the sea state was usually dominated by swell waves that propagated from the southeast and exhibited little dependency on the local wind. During the experiment, the angle between wind and dominant wave θ ranged from the same direction (θ less than 20°) to virtually the opposite direction ($\theta > 160°$).

Figure 2c shows the significant wave height Hs and the significant swell wave height Hs_{swell}. Hs_{swell} was calculated by the same method as that used by Smedman et al. (2003), which is based on wave spectra. The significant swell wave height occupied a large portion of the total significant wave height in many runs, indicating the dominant position of swell waves.

Figures 2d and 2e show the longitudinal component τ_x and the lateral component τ_y of the wind stress. Figure 2f shows the spectrogram of the surface displacement $S_{\eta\eta}$. The frequency of dominant waves mostly remained between 0.09 and 0.2 Hz.

The stability parameter z/L in Fig. 2g shows that both stable and unstable conditions were encountered. The large-eddy simulation (LES) by Wu et al. (2017) showed that the swell wave effect on the MABL can be influenced by the buoyancy force, and therefore, in order to study the turbulence within the MABL, it is better to exclude the influence of the buoyancy because the AEM is derived under neutral conditions. Therefore, runs in near-neutral stratification (defined here as $z/|L| < 0.1$) were selected for analysis.

Before the analysis of the measurements, runs with winds from the northwest quadrant (i.e., winds coming from behind the tower or from the small islands) were excluded in order to reduce possible distortion effects. Reasonably stationary conditions were also checked: runs that exhibited large changes in either wind speed or direction were rejected because they may encounter the inertial boundary layer (IBL). To ensure sufficient statistical reliability of the results, runs with extreme conditions (e.g., very large or small wind speed) were not included in the analysis.

After applying these stringent criteria, we confirmed whether the measurements were within the WBL by using the velocity spectra (section 3a). We observed that under wind-sea conditions, all measurements were above the WBL because the velocity spectra had no wave-related peak. However, in the presence of a fast swell, the wave-induced perturbation extended much higher. To analyze the influence of the swell on the wind profile, only one measurement height (i.e., 8 m, the lowest observational level) with significant

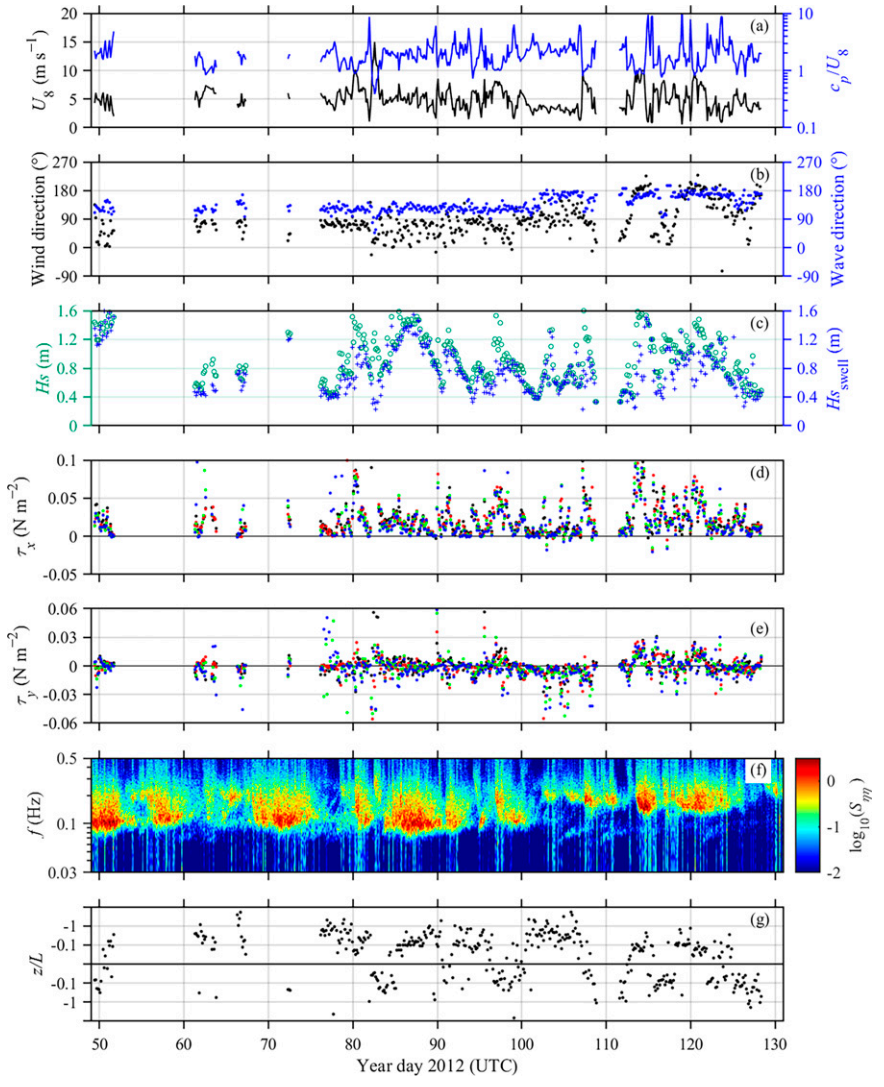

FIG. 2. Time series of meteorological and surface wave parameters. (a) Wind speed at 8 m and wave age c_p/U_8. (b) Wind and wave direction. (c) Significant wave height Hs and significant swell wave height Hs_{swell}. (d),(e) Four-level wind stress components τ_x and τ_y, respectively, and stress components at 8, 20, 28, and 36 m are black, red, green, and blue points, respectively. (f) Spectrogram of the surface displacement. (g) Atmospheric stability parameter z/L.

wave-related spectral peaks was selected. This is because (i) measurements at the upper three levels can be used to verify whether the wind profile above the WBL meets the logarithmic law, and (ii) if the logarithmic law appears in the wind profile above the WBL, as suggested by Edson and Fairall (1998) and Zou et al. (2020), then this logarithmic profile can be used as a reference to determine how the mean wind deviates from it within the WBL. Then, we selected three kinds of cases: wind-sea conditions ($c_p/U_8 < 1.2$ and $\theta < 45°$), wind-following swell conditions ($c_p/U_8 > 1.2$ and $\theta < 45°$) when swell exerted upward wave-induced stress, and wind-opposite swell conditions ($c_p/U_8 > 1.2$ and $\theta > 135°$) when swell absorbed energy from the MABL. The number of runs classified as each condition was 38, 37, and 18, respectively.

In a large proportion of the runs, we found the wind was blowing from the northeast sector. The offshore wind may be affected by the IBL (e.g., Mahrt et al. 2016; Fairall et al. 2006), while the generation of wind waves can be affected by the slanting-fetch effect (e.g., Ardhuin et al. 2007).

For the IBL, the turbulence generated over the rigid land surface differs from the turbulence over the water surface, leading to a distinct discontinuity of the wind profile above the IBL (because the wind profile both within and out of the IBL follows a logarithmic law but depends on different wind stress). Our observation (shown in Figs. 6–8) showed that the wind profiles follow a logarithmic law under wind-sea conditions. Under swell conditions, although the wind profiles showed distinct discontinuities, they did not follow a logarithmic law.

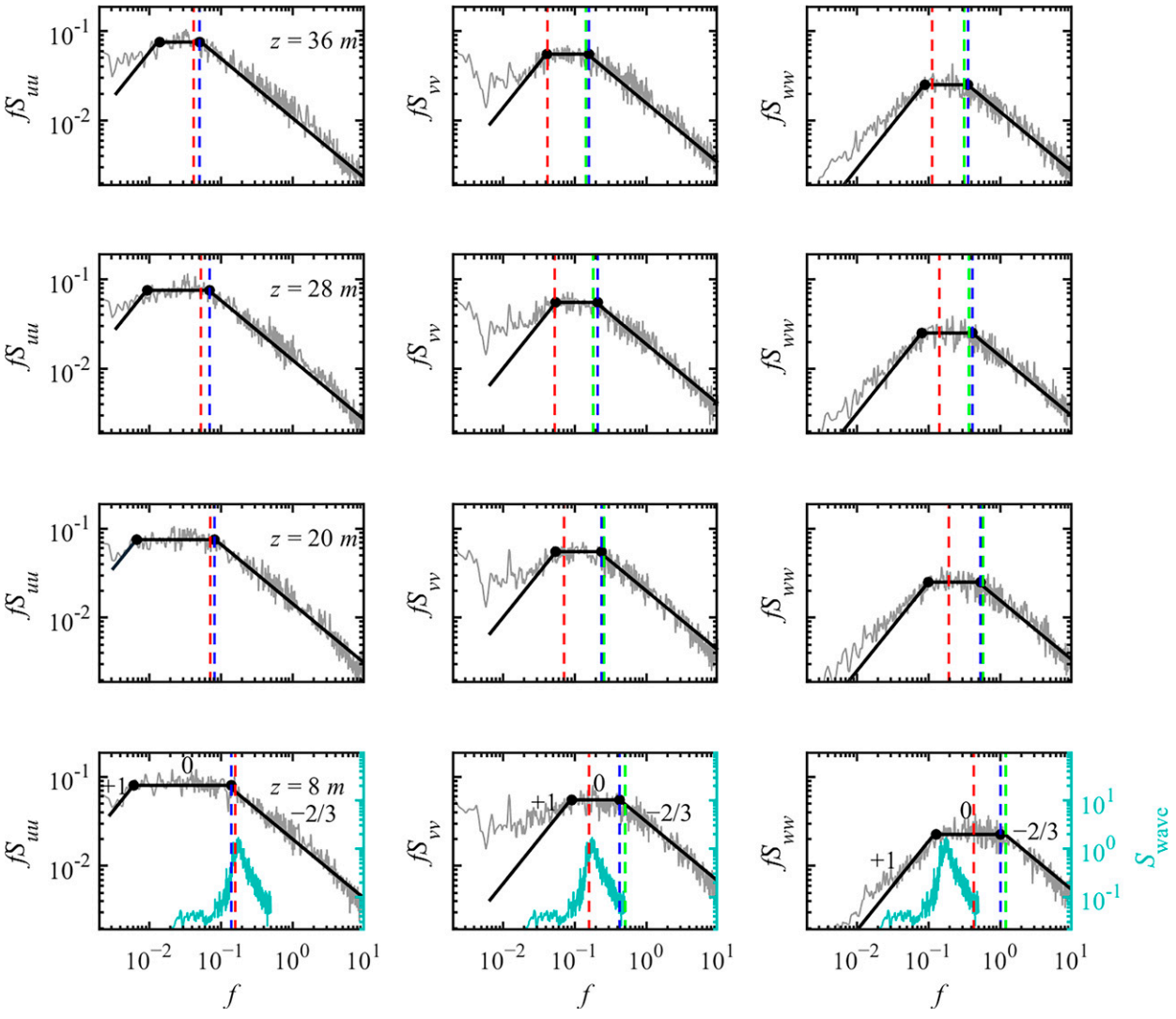

FIG. 3. Premultiplied velocity spectra under wind-sea conditions (for the run: yearday 121, 0500 UTC, with $U_8 = 8.0$ m s^{-1}, $c_p/U_8 = 1.1$, $\theta = 17°$, Hs = 1.1 m, and $\mathrm{Hs}_{\mathrm{swell}} = 0.6$ m). The (left) longitudinal, (center) lateral, and (right) vertical velocity spectra (fS_{uu}, fS_{vv}, and fS_{ww}, respectively) are plotted against frequency f (gray lines). (from bottom to top) Spectra at 8, 20, 28, and 36 m, respectively; the dark green line in each bottom panel represents the wave spectrum. The black lines indicate the slopes of the spectra and are marked with "−2/3", "0," and "+1" in the bottom panels. The black filled circles represent the lower and higher limits of the f^0 subrange. The vertical red dashed lines show $f = a_1U/(2\pi z)$ [Eq. (2)] with $a_1 = 1$ for fS_{uu} and fS_{vv}, and $f = b_1U/(2\pi z)$ [Eq. (2)] with $b_1 = 2.7$ for fS_{ww}. The vertical green dashed lines represent $f = a_1U/(2\pi z)$ with $a_1 = 1$ and 3.4 for fS_{uu} and fS_{vv}, respectively, and $f = b_1U/(2\pi z)$ with $b_1 = 7.5$ for fS_{ww}. The vertical blue dashed lines show the real transition frequency from the −5/3 to −1 power-law region for S_{ii}. In fS_{uu}, the green lines are mixed with blue lines.

These findings rule out the IBL effect. The slanting-fetch effect can cause the direction of wind waves to differ from the wind direction by several tens of degrees. This can be seen in Fig. 2b for $c_p/U_8 < \sim 1.2$. Since the water was not deep (~16 m), it was also important to check for breakers. It is widely accepted that waves break when steepness $k_p\mathrm{Hs}/2$ is larger than 0.44 ~ 0.55 (Toffoli et al. 2010), where k_p is the wave spectral peak wavenumber. We computed the wave steepness and found that it ranged from 0.01 to 0.08, which is well below than the criterion for breakers.

3. Results

a. Observed velocity spectra

To better understand the turbulence and wave-induced perturbations within the MABL, the spectra of the three-dimensional wind velocity fluctuations, i.e., the longitudinal, lateral, and vertical velocity energy spectra (fS_{uu}, fS_{vv}, and fS_{ww}, respectively), at four measurement levels were analyzed. Figures 3–5 display the typical premultiplied frequency spectra on a log–log scale (other spectra used in this study can be found in the online supplemental material). They are examples

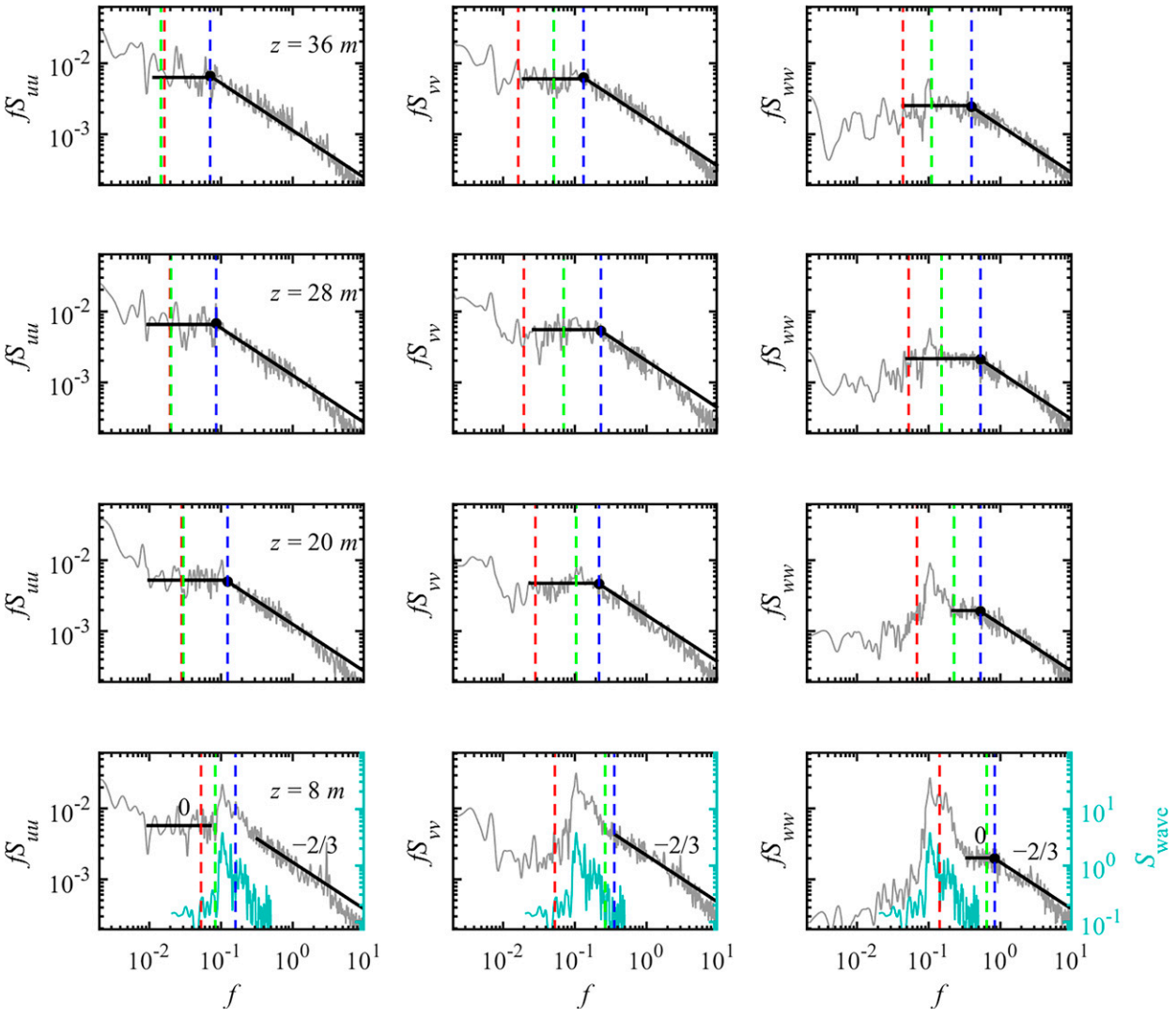

FIG. 4. As in Fig. 3, but for wind-following swell conditions (for the run: yearday 52, 1400 UTC, with $U_8 = 2.7$ m s^{-1}, $c_p/U_8 = 3.6$, $\theta = 43°$, and $\mathrm{Hs}_{\mathrm{swell}} = 1.7$ m) and the vertical green dashed lines representing $f = a_1|U - c\cos\theta|/(2\pi z)$ with $a_1 = 1$ and 3.4 for fS_{uu} and fS_{vv}, respectively, and $f = b_1|U - c\cos\theta|/(2\pi z)$ with $b_1 = 7.5$ for fS_{ww}.

of the velocity spectra under wind sea, wind-following swell, and wind-opposite swell conditions, respectively. The wave spectra are also plotted in the bottom panels to assess the impact of surface waves on the wind velocity spectra.

1) SPECTRAL SHAPE

Under wind-sea conditions, the observed velocity spectra fell into three regions (Fig. 3): (i) a high-frequency range where fS_{ii} follows the $-2/3$ power law (the inertial subrange and $-5/3$ power law for S_{ii}); (ii) an intermediate-frequency range where fS_{ii} is constant (the production range of turbulence and -1 power law for S_{ii}); and (iii) a low-frequency range where fS_{ii} is proportional to f (the very large-scale motion and S_{ii} is constant). The longitudinal spectrum fS_{uu} at 8 m exhibited a very long and clean plateau which extends almost a decade and a half in frequency, and it may be the longest -1 power-law region reported in the literature (Calaf et al. 2013).

Figures 4 and 5 show the velocity spectra when the sea state was dominated by swell waves. Similar to in Fig. 3, they all have a clear inertial subrange annotated with "$-2/3$," except for a peak at the low-frequency end of the f^{-1} region, ranging from 2×10^{-2} to 4×10^{-2} Hz, which was exerted by the very large-scale motion (Guala et al. 2006) and dampened with decreasing height for fS_{uu}. In the dominant wave frequency, another peak appeared in the intermediate-frequency range of spectra at 8 m. The appearance of these peaks shortened the plateaus.

Drobinski et al. (2004) and Drobinski et al. (2007) showed that the -1 power law was absent in S_{ww} within the eddy surface layer which was the lower sublayer of the ABL lying between the surface and approximately 20 m in height. It is

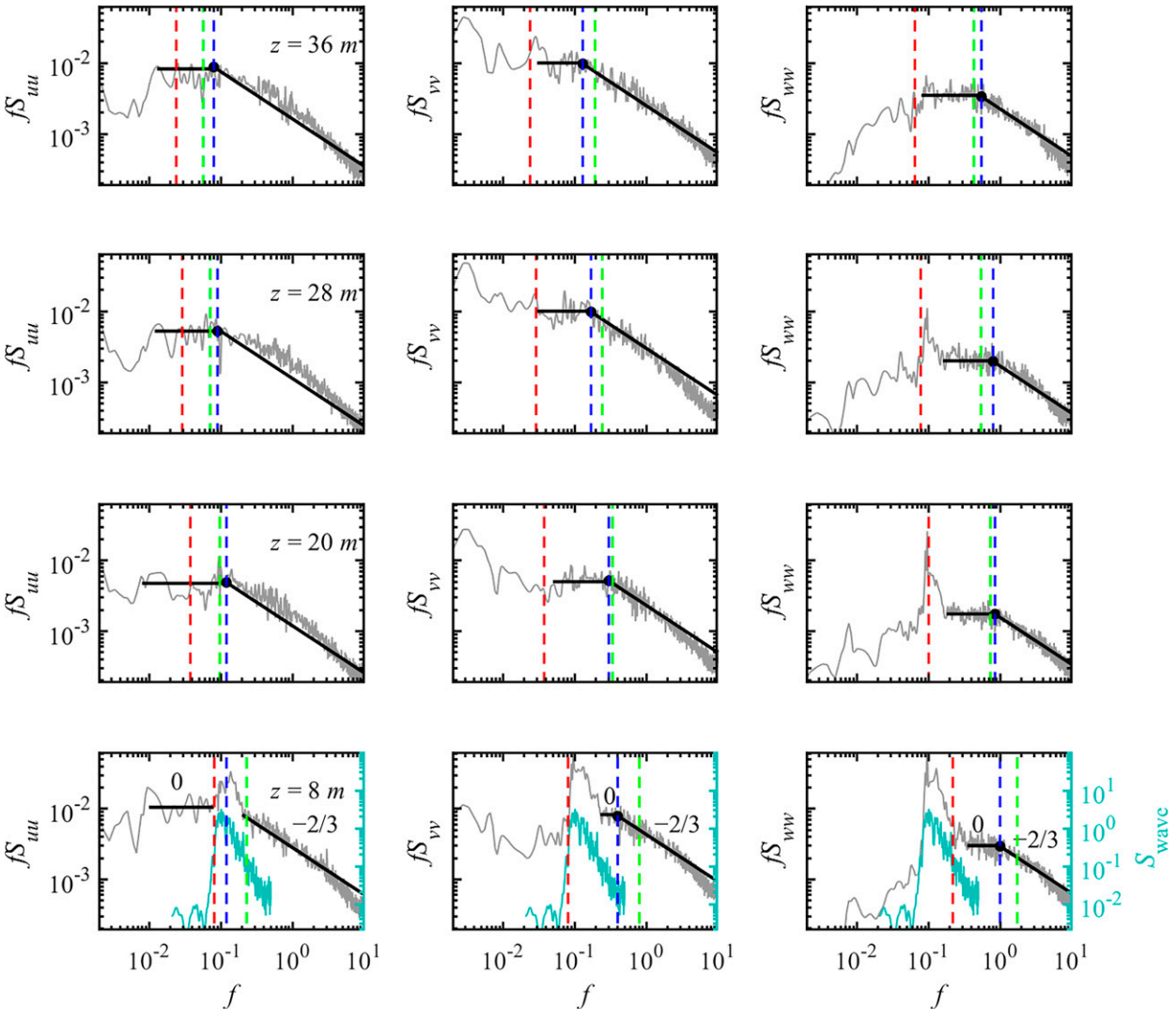

FIG. 5. As in Fig. 4, but for wind-opposite swell conditions (for the run: yearday 87, 2000 UTC, with $U_8 = 4.1$ m s^{-1}, $c_p/U_8 = 2.4$, $\theta = 139°$, and $\mathrm{Hs}_{\mathrm{swell}} = 1.4$ m).

further demonstrated by Ghannam et al. (2018) that the -1 power law did not appear in the vertical spectra except at large distances from the surface. However, our study showed that S_{ww} had a clear -1 power-law region at 8 m, which is much lower than 20 m.

The theory predicts that the transition frequency from the inertial subrange to the -1 power-law region in the horizontal velocity spectra occurs at $kz \sim 1$ or $f \sim U/(2\pi z)$ [Eqs. (1) and (2)]. Under wind-sea conditions, the transition frequency occurred at $kz \approx 1$ in the longitudinal spectra but not in the lateral spectra, and specifically, the actual transition point in the lateral spectra is $kz \approx 3.4$ or $f \approx 3.4U/(2\pi z)$, which is higher than that obtained from a rigid land surface. Drobinski et al. (2004) showed that over a rigid land surface, $f \approx 0.43U/z$ or $f \approx 2.7U/(2\pi z)$ set the transition in the vertical spectra, while our data showed that the transition commenced at $f \approx 7.5U/(2\pi z)$, which may differ from their result due to the undulation of the ocean surface. For the wind-following swell condition, Fig. 4 shows that the transition points occurred at $f \approx 5.3U/(2\pi z)$ for fS_{uu}, $f \approx 9.5U/(2\pi z)$ for fS_{vv}, and $f \approx 22U/(2\pi z)$ for fS_{ww}, and this result was obviously different from that of wind seas. Under wind-opposite swell conditions, Fig. 5 shows that the transition points occurred at $f \approx 3.3U/(2\pi z)$ for fS_{uu}, $f \approx 7.2U/(2\pi z)$ for fS_{vv}, and $f \approx 21U/(2\pi z)$ for fS_{ww}.

In addition to the three spectral ranges [Eqs. (1) and (2)], a fourth range, which represents the mesoscale motion (Högström et al. 2002), at even lower frequencies, can be observed in fS_{vv} of Fig. 3. This range was more pronounced under swell conditions (the fourth range is not marked by a black line with a slope number in Figs. 3–5). Under swell conditions, the frequency of high-amplitude noise in cospectra induced by mesoscale motion was up to 10^{-2} Hz in our observation. Mesoscale fluctuations can cause serious contamination in flux calculations

(Vickers and Mahrt 2003; Kudryavtsev and Makin 2004), and thus, they have been widely excluded (Smedman et al. 2009; Li et al. 2020). The mesoscale motion can also influence the +1 range (very large-scale motion) by partly masking it (Figs. 4 and 5).

2) SWELL-INDUCED SPECTRAL PEAK

Figures 4 and 5 show that, compared with the velocity spectra under wind-sea conditions, special peaks appeared at the frequency of the dominant wave, corresponding to wave-induced perturbations that were phase locked with the wave (Hristov et al. 1998). This phenomenon has also been reported by previous studies (e.g., Soloviev and Kudryavtsev 2010; Högström et al. 2015; Zou et al. 2020). According to the shear instability (Miles 1957; Hristov et al. 2003; Wu et al. 2018), wave-induced perturbations decrease with increasing height, and horizontal components decay more rapidly than the vertical component. Figures 4 and 5 show that the peak in the vertical spectra was more pronounced than the peak in the lateral or longitudinal spectra at 8 m. In the vertical spectra, the swell-induced peak was still strong at a height of 20 m, and a weak peak was observed even at 28 m. These features are consistent with the shear instability.

b. *Momentum flux and wind profile*

1) WIND-SEA CONDITIONS

Under wind-sea conditions, as shown in Fig. 3, all measurement heights were above the WBL, i.e., there were no perturbations induced by waves, and thus, the wave-induced stress was zero. The near-neutral ABL indicated that the mean wind speed over wind seas should follow the logarithmic profile [Eq. (3)]. Figure 6a shows the mean wind profiles under wind-sea conditions in a representation with U on a linear scale and z on a logarithmic scale. It can be seen that winds met the logarithmic height dependence. This agrees with Smedman et al. (2003), who showed that the measured wind profiles over wind seas can be normalized by using MOST. An example of *uw* cospectra $f\mathrm{Co}_{uw}$ at heights of 8 and 20 m, corresponding to one of the gray lines in Fig. 6a, is also given in Fig. 6b, which shows downward momentum fluxes for all frequency bins under wind-sea conditions.

2) WIND-FOLLOWING SWELL CONDITIONS

The wind profiles when wind follows the swell are shown in Fig. 7a to assess the influence of the swell wave. The figure shows that the profiles had the same features: (i) the wind profile nearly followed a straight line for the upper three levels (20, 28, and 36 m), implying that the mean wind followed the logarithmic profile above the WBL; and (ii) the wind speed at 8 m deviated to the left of the logarithmic profile satisfied above 8 m, i.e., within the WBL, the wind gradient was larger than that obtained by extrapolation using the logarithmic profile above. This phenomenon is consistent with previous studies, e.g., Smedman et al. (2009), who found a distinct knee in the wind profile under wind-following swell conditions.

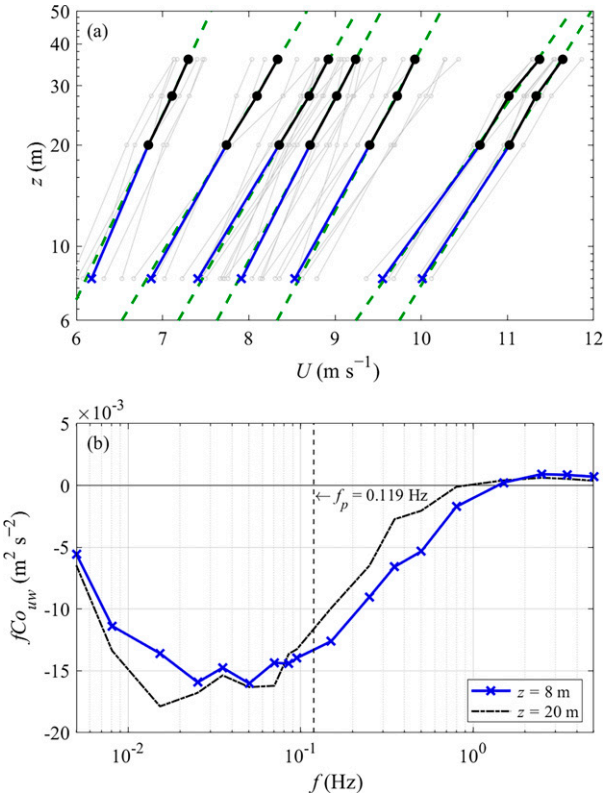

FIG. 6. Mean wind profiles and *uw* cospectra ($f\mathrm{Co}_{uw}$) under wind-sea conditions. (a) The 30-min-mean wind profiles are plotted with U on a linear scale and z on a logarithmic scale. Gray lines represent all individual wind-sea runs. The bold circle-cross lines represent bin-averaged profiles. The green dashed lines represent the best fit to Eq. (10). (b) An example of *uw* cospectra (for the run: yearday 114, 2300 UTC, with $U_8 = 7.7$ m s^{-1}, $c_p/U_8 = 1.1$, $\theta = 23°$, Hs = 1.5 m, and $\mathrm{Hs}_{\mathrm{swell}} = 1.1$ m) at 8 and 20 m are plotted with f on a logarithmic scale and $f\mathrm{Co}_{uw}$ on a linear scale, and the dashed line represents the frequency of the dominant wave (f_p). The run plotted in (b) corresponds to one of the gray lines in (a).

In the presence of swell waves, the large wind gradient within the WBL has been extensively studied (Hanley and Belcher 2008; Song et al. 2015; Wu et al. 2017). In their analyses, Nilsson et al. (2012) and Högström et al. (2018) found that this is due to the upward momentum exerted by swell. Figure 7b gives the *uw* cospectra at heights of 8 and 20 m. It shows that at a height of 8 m, a distinct positive peak, suggesting upward momentum (Kahma et al. 2016), occurred at the frequency of the dominated wave (peak wave frequency $f_p = 0.098$ Hz). However, above the WBL, the *uw* cospectra at 20 m was similar to the 11-m observation in Grachev and Fairall's (2001) Fig. 7, which was based on the SCOPE observations.

3) WIND-OPPOSITE SWELL CONDITIONS

In this section, the cases of swell traveling against wind are shown. Similar to Fig. 6, the wind profiles and *uw* cospectra are given in Figs. 8a and 8b, respectively.

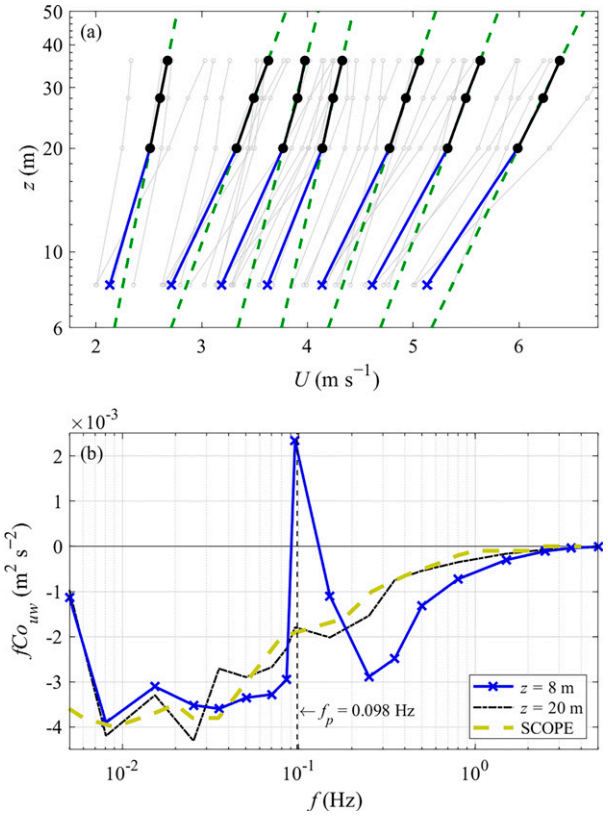

FIG. 7. As in Fig. 6, but for wind-following swell conditions. An example of *uw* cospectra (for the run: yearday 51, 1400 UTC, U_8 = 4.2 m s^{-1}, c_p/U_8 = 2.3, θ = 40°, and Hs_{swell} = 1.6 m) are plotted in (b).

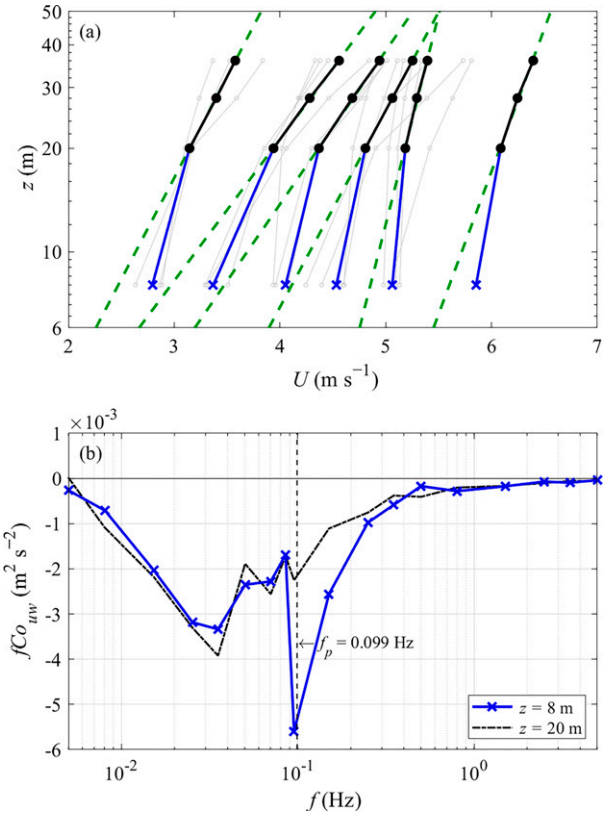

FIG. 8. As in Fig. 6, but for wind-opposite swell conditions. An example of *uw* cospectra (for the run: yearday 51, 1700 UTC, U_8 = 2.9 m s^{-1}, c_p/U_8 = 3.3, θ = 141°, and Hs_{swell} = 1.4 m) are plotted in (b).

Figure 8a shows that the mean wind followed a logarithmic profile above 20 m, but within the WBL, in contrast with Fig. 7a, the wind speed was greater than the extension of the logarithmic profile obtained by fitting to the wind speeds above the WBL. Similar to the wind-following swell condition (Fig. 7b), the *uw* cospectrum at 8 m showed a strong peak around the swell frequency (f_p = 0.099 Hz). However, in this case, the peak was negative, suggesting a downward momentum flux, i.e., the swell wave absorbed energy from the wind.

c. *Turbulence variances*

Figure 9 shows the profiles of the normalized longitudinal, lateral, and vertical turbulence variances (or turbulence intensities). Note that within the WBL, the turbulence variances were normalized by τ_t/ρ instead of τ/ρ, while $\tau/\rho = \tau_t/\rho$ above the WBL or in the terrestrial ABL, i.e., to make comparisons with the boundary layer flow over wind seas and rigid surface, the "turbulent friction velocity" should be used. To remove the wave effect from the total wind stress and velocity variances, the turbulent stress and turbulence variances were derived following Högström et al. (2015). Figure 9a shows that under wind-sea conditions, the longitudinal and lateral turbulence variances decreased with increasing height, and the profile was nearly a straight line, following Eq. (3), while the vertical turbulence variance roughly increased with height following $z^{2/3}$ [Eq. (4b)]. The logarithmic variation of the horizontal turbulence variances was consistent with the land observation by Drobinski et al. (2004) and the cold-front study of Huang et al. (2021).

Huang et al. (2021) showed that, when light wind follows the swell wave, the variation of the turbulence variances differs from that over wind seas; the magnitude of the turbulence variances is much larger within the WBL, and they decrease at first and then increase with height above the WBL. In Figs. 9b and 9c, the variation of the turbulence variances with height for the wind-following and -opposite swell are shown. It is obvious that the turbulence variances have their own distinct features compared with cases under wind-sea conditions. For wind-following swell conditions, the three components of the turbulence variance sharply decreased from 8 to 20 m but increased above 20 m. For wind-opposite swell conditions, the turbulence variances are similar to those over the wind sea except for deviation of turbulence variances from the log profile at 8 m.

4. Analysis of the results

The turbulence within the ABL covers a very large range of sizes, ranging from the smallest eddies set by the viscosity to the largest scale set by the height of the boundary layer. Among these eddies, the Kolmogorov region, which follows

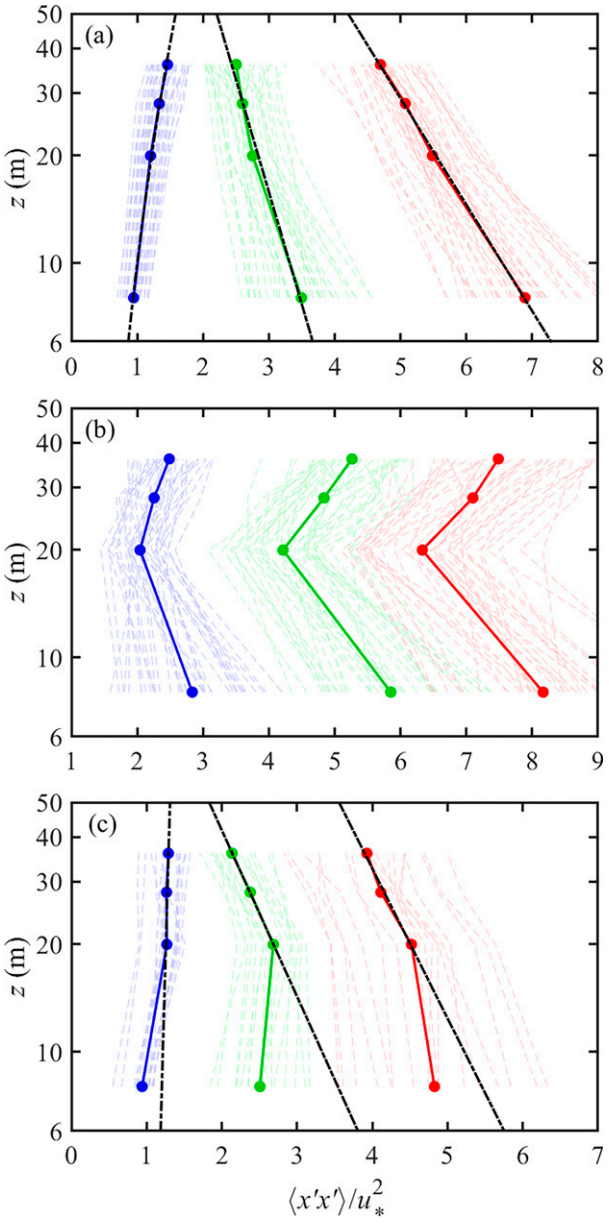

FIG. 9. Profiles of the nondimensional turbulence variances under the conditions of (a) wind sea, (b) wind-following swell, and (c) wind-opposite swell. The profiles are plotted in log-line representation. The light red, light green, and light blue dashed lines represent the profiles of the longitudinal, lateral, and vertical turbulence variances, respectively, of all individual runs. The bold red, green, and blue lines with filled circles represent the mean profiles of the longitudinal, lateral, and vertical turbulence variances, respectively. The black dash–dotted lines in (a) and (c) are the best fit to Eq. (3) for the horizontal turbulence variances and are the best fit to Eq. (4b) for the vertical turbulence variance.

the −5/3 law, attracts attention because it is a basic method used to compute the air–sea flux on a shaking platform. Studies of eddies that are larger than the Kolmogorov scale, which is directly linked with the mean wind profile, have been limited. The logarithmic law of the mean wind profile is widely adopted in oceanic and atmospheric models (e.g., García-Nava et al. 2009) and used to determine the air–sea flux (Drennan et al. 2007). In this section, the turbulence characteristics under the influence of waves are analyzed.

a. Wind-sea conditions

Perry's AEM, developed over the rigid surface, depicts the energy-containing eddies as Λ vortexes that have a fixed angle of inclination. Based on the overlap argument that both the "inner flow" and "outer flow" scaling laws are valid, the horizontal spectra within $(a_1 z^{-1} H^{-1})$ follow the k^{-1} (f^{-1}) law. The idea behind the AEM is that only those eddies with a scale of z contribute efficiently to turbulence intensities, which is very similar to the widely used Prandtl's mixing length [Eq. (10)]. The validation of the k^{-1} law has been widely examined in the laboratory and over the rigid land surface but rarely over undulated surface waves (Smedman et al. 2003). Our observation shows that the MABL also contains attached eddies (Fig. 3).

Miles's (1957) shear instability shows that the generation of surface waves can be expressed as

$$\overline{\tilde{u}\tilde{w}} \frac{\partial U}{\partial z} + \frac{1}{\rho} \frac{\partial \overline{\tilde{w}\tilde{p}}}{\partial z} = 0, \tag{11}$$

where p is the air pressure, which represents the work done by the wave-induced pressure on the surface and wave-induced stress extracted from the wind shear. The wave-induced stress at a given height z depends on the wind speed (the wave-induced stress can extend to height z, where the wind speed is equal to the wave phase speed) and wave height (Hristov and Ruiz-Plancarte 2014). Our data showed that a lower wave age together with a low wave height led to the insignificant wave-induced peak in the velocity spectra under wind-sea conditions (Fig. 3). Under these conditions, the velocity spectra and the turbulence variances were similar to those over a rigid surface. The effective eddies followed the −1 power law, and the transition frequency from the inertial subrange to the f^{-1} region in the longitudinal velocity spectra followed Eq. (1), leading to the logarithmic profile of the horizontal turbulence variances and demonstrating the validity of MOST.

b. Swell conditions

Under swell conditions when the wave state was not in equilibrium with the local wind, our data showed that the features of the wind profile and turbulence structure were quite different from those over the wind sea and land. Under these conditions, the Taylor–Goldstein equation $d^2\phi/dz^2 - [k^2 + \partial_z^2 U/(U-c)]\phi = 0$ did not exhibit singularity, and thus the swell wave did not extract energy from wind shear directly through vortex force [Eq. (11)]. Its effect on the MABL was through the pressure difference before and behind the wave crest (details can be found in section 5). Because the AEM corresponds to the logarithmic wind profile, the distinct turbulent features can help us to illustrate the deviation of the wind profile modulated by swell.

For the wind-following swell cases, Fig. 7b shows that there was a positive peak in the *uw* cospectra, indicating the upward momentum flux exerted by pressure near the swell surface. In this case, the longer f^{-1} plateau within the WBL corresponded to the larger wind gradient shown in Fig. 7a, i.e., to balance those negative wave-induced stress and to make the total flux within the MABL constant, the turbulence stress within the WBL should increase. The longer f^{-1} plateau also led to a larger turbulence variance at a height of 8 m [Eqs. (3) and (4)], as seen in Fig. 9b.

Equation (2) is used to separate the −5/3 power law and the −1 power law region over the rigid surface. Considering the relative speed between wind and the swell and the angle difference, it is optimal to replace the wind speed in Eq. (2) as $|U - c\cos\theta|$. In Fig. 4, the vertical green dashed lines represent $f = a_1|U - c\cos\theta|/(2\pi z)$ and $f = b_1|U - c\cos\theta|/(2\pi z)$ for the horizontal velocity spectra and vertical velocity spectra, respectively, and the values of a_1 and b_1 were taken from that over wind seas. The result showed that the transition point was slightly shifted to the right side of the vertical line even though it did not fully match the transition point. This was due to the higher wave-induced pressure: the attached eddies were redistributed, i.e., the eddies near the wave peak were lifted to reach a higher position. This suggests that the height z not only contained attached eddies that had the scale of z but also included the other scale attached eddies.

It is also interesting to assess whether the redistributed attached eddies can affect the Prandtl mixing length. We found that the upper three levels of wind speed had a logarithmic shape, suggesting that although the turbulence variances were different from those under wind-sea conditions, the lifted attached eddies had less effect on momentum flux because those attached eddies concentrated near the wave peak frequency region and thus accounted for a smaller portion of the total momentum flux.

The opposite was true for the wind-opposite swell cases. Due to the positive wave-induced stress accounting for part of the total stress, the turbulent stress was small. As a result, the wind gradient and the turbulence variances were reduced, which was similar to the profile near the surface over wind seas (e.g., Fig. 3 in Babanin et al. 2018).

As with that for the wind-following swell condition, the vertical green dashed lines based on the relative speed $|U - c\cos\theta|$ are plotted in Fig. 5. They roughly separate the −5/3 power law and the −1 power law above the WBL, but the f^{-1} region was shorter than that predicted within the WBL (Fig. 5). This suggests that the effect of the wind-opposite swell on the turbulence above the WBL was similar to other topography except for its movement causes the relative speed. For the turbulence within the WBL, however, the shorter f^{-1} plateau corresponded to the small wind gradient and led to small values of the turbulence variances.

5. Discussion

During the wind sea, where the wave phase speed was small, almost all our measurements were above the wind-sea WBL, and only a few data points observed the wave-induced perturbations at a height of 8 m; thus, they were not analyzed in our study. However, under hurricane conditions, most of the wind speed observed by buoys is within the wind-sea WBL and is then extrapolated to the standard height based on MOST. If MOST is not valid under those conditions, as shown by Babanin et al. (2018), then its application can result in many unknowns. For example, Voermans et al. (2019) recently observed that the wind stress derived based on the logarithmic profile was different from that observed with the eddy covariance method.

The LES studies of Zhang et al. (2019) and Wang et al. (2021) showed that at the wave-induced stress dominated height, the wind profile moved to the left side of the logarithmic profile. They also showed that the MABL retained but redistributed geometric self-similarity eddies in the presence of wind seas, except for the weakened small-scale attached eddies and the enhanced large-scale attached eddies. However, the reconstructed eddies followed the logarithmic law above the WBL. These features are similar to those in our data regarding wind seas.

Based on several experiments, Högström et al. (2015) found that the drag coefficient obtained from TOGA COARE, the Rough Evaporation Duct (RED), and the San Clemente Ocean Probing Experiment (SCOPE) was significantly larger than that obtained from the Baltic Sea Swell Experiment (BASE). Further analysis showed that this was induced by the momentum flux absorbed by the swell, even under wind-following swell conditions. A reviewer speculated that "misalignment of wind and swell would lead to the observed downward momentum of swell." However, they found no correlation between wind and wave propagation. Högström et al.'s observation seems to contradict our results. However, other data showed that swell exerted upward momentum and that a transition occurred at $U_7 = 4$ m s^{-1} (Högström et al. 2018). After reviewing the dataset used in their 2015 study, we found that the downward momentum induced by wind-following swells might be due to the small wave age. Our data also showed that when the wave age is not large enough, the swell absorbed energy from the MABL. The mechanics behind this can be explained as follows.

For surface wave $\eta = -iae^{ik(x-ct)}$, the wave-induced perturbations induced by the wave-induced pressure are $\tilde{u} = \hat{u}e^{ik(x-ct)}$ and $\tilde{w} = \hat{w}e^{ik(x-ct)}$, where hat/circumflex represents amplitude. Using Eq. (11), we obtain

$$(\hat{u}^*\hat{w} + \hat{u}\hat{w}^*)\frac{\partial U}{\partial z} = -\frac{1}{\rho}\frac{\partial(\hat{w}^*\hat{p} + \hat{w}\hat{p}^*)}{\partial z}, \tag{12}$$

where asterisk represents the conjugate complex number. For the wind-following swell when the wave age is relatively small, the structure of wave-induced pressure is similar to that over a wind sea, that is, $\tilde{p} = \hat{p}e^{ik(x-ct)}$, which means that the high pressure on the windward side still acts at the surface to transfer energy from the atmosphere to the wave. However, when the wind speed is lower or the wave phase speed is larger than the maximum wind speed within the ABL, field observation (Kahma et al. 2016) and LES studies (Sullivan et al. 2008; Cao and Shen 2021) have shown that the wave-induced pressure

shifts from that over wind seas. The image parts of $\hat{u}$ and $\hat{w}$ are generated by viscosity. The work is done by the swell and thus there is high pressure on the leeward side: $\tilde{p} = (\hat{p}e^{i\pi})e^{ik(x-ct)}$. Inserting the phase-shifted wave-induced pressure into Eq. (12), we find that the wave-induced stress changes sign because $\partial U/\partial z$ is always positive within the WBL, indicating upward wave-induced stress for a large wave age of wind-following swell waves. This opposite effect is exhibited in wind-opposite swell conditions because the pressure structure is retained similarly to that over wind seas, leading to the downward wave-induced stress (Cao et al. 2020).

To study the turbulence distorted by surface waves, Townsend (1972) obtained the wind gradient $dU/dz = u_{*t}^3(z)/u_*^2\kappa z$ by specifying the turbulent-dependent energy dissipation. Although Townsend's equation is slightly different from that of Makin and Kudryavtsev (1999), both showed that wave-induced stress could result in the departure of the wind profile from the logarithmic law. Our analysis showed that due to the special link between wind shear and the attached eddy, whether within or above the WBL, the turbulent stress should be used, i.e., the wind profile should be $U = u_{*t}(z)/\kappa \ln(z/z_0)$.

6. Conclusions

Field observations from the South China Sea were used to study the characteristics of the MABL under the influence of ocean surface waves. The turbulence measurements were made at four heights above the surface (8, 20, 28, and 36 m), providing the feasibility of studying the variation of the wave effect with height. After applying strict quality control procedures, we analyzed three conditions under near-neutral atmospheric stratification: wind-sea, wind-following swell, and wind-opposite swell.

Under wind-sea conditions, when the measurements are above the shallow WBL, the MABL was dominated only by shear-generated turbulence, which is similar to results reported from the laboratory and the terrestrial ABL. Under these conditions, the logarithmic height dependence of the wind profile was observed, and the velocity spectra and the turbulence variances closely followed the AEM, suggesting that MOST is valid over wind seas. In addition, for the longitudinal spectra, the transition frequency from the inertial subrange (the $-5/3$ power law) to the production range of turbulence (the -1 power law) occurred precisely where predicted theoretically at $kz = 1$ [Eq. (1)], providing solid empirical evidence for the existence of the k^{-1} law in the MABL flows.

When swell dominated the sea state, distinct peaks were observed in the velocity spectra. Our data showed that the MABL also contained attached eddies, but that the transition point from the inertial subrange to the -1 power-law region was different from that of wind seas due to the modification of swell waves, leading to the distinct features of the f^{-1} plateau, the turbulence variances, and the mean wind profile.

When swell traveled in a direction similar to the wind and exerted upward momentum flux, the wind gradient became larger within the WBL than that of the extrapolation based on the logarithmic profile above the WBL. Under these conditions, the length of the f^{-1} plateau was longer, and the turbulence variances were considerably large. However, when swell absorbed energy from the wind (the wind-opposite swell), the wind gradient was smaller than the extrapolation, the length of the f^{-1} scaling region and the turbulence variances also showed the opposite results of wind-following swell cases.

Acknowledgments. This work was supported by the National Natural Science Foundation of China (41830533, 41806028, 41606024); the National Basic Research Program of China, Monitoring and Forecasting of Finescale Structure and Impact Assessment of Landfalling Typhoons (2015CB452800); and the Construction Project of the National Climate Observatory of the China Meteorological Administration.

Data availability statement. The data used in this study is available from Changlong Liu (clliu@zju.edu.cn) at Ocean College, Zhejiang University, and Zhongshui Zou (zouzhsh3@mail.sysu.edu.cn) at Ocean College, Zhejiang University, and School of Marine Science, Sun Yat-Sen University.

REFERENCES

Ardhuin, F., T. H. C. Herbers, G. P. van Vledder, K. P. Watts, R. Jensen, and H. C. Graber, 2007: Swell and slanting-fetch effects on wind wave growth. *J. Phys. Oceanogr.*, **37**, 908–931, https://doi.org/10.1175/JPO3039.1.

Babanin, A. V., J. McConochie, and D. Chalikov, 2018: Winds near the surface of waves: Observations and modeling. *J. Phys. Oceanogr.*, **48**, 1079–1088, https://doi.org/10.1175/JPO-D-17-0009.1.

Balakumar, B. J., and R. J. Adrian, 2007: Large- and very-large-scale motions in channel and boundary-layer flows. *Philos. Trans. Royal Soc.*, **A365**, 665–681, https://doi.org/10.1098/rsta.2006.1940.

Banerjee, T., and G. G. Katul, 2013: Logarithmic scaling in the longitudinal velocity variance explained by a spectral budget. *Phys. Fluids*, **25**, 125106, https://doi.org/10.1063/1.4837876.

Buckley, M. P., and F. Veron, 2016: Structure of the airflow above surface waves. *J. Phys. Oceanogr.*, **46**, 1377–1397, https://doi.org/10.1175/JPO-D-15-0135.1.

Calaf, M., M. Hultmark, H. J. Oldroyd, V. Simeonov, and M. B. Parlange, 2013: Coherent structures and the k^{-1} spectral behaviour. *Phys. Fluids*, **25**, 125107, https://doi.org/10.1063/1.4834436.

Cao, T., and L. Shen, 2021: A numerical and theoretical study of wind over fast-propagating water waves. *J. Fluid Mech.*, **919**, 38, https://doi.org/10.1017/jfm.2021.416.

——, B. Deng, and L. Shen, 2020: A simulation-based mechanistic study of turbulent wind blowing over opposing water waves. *J. Fluid Mech.*, **901**, 27, https://doi.org/10.1017/jfm.2020.591.

Chen, S., F. Qiao, W. Jiang, J. Guo, and D. Dai, 2019: Impact of surface waves on wind stress under low to moderate wind conditions. *J. Phys. Oceanogr.*, **49**, 2017–2028, https://doi.org/10.1175/JPO-D-18-0266.1.

del Álamo, J. C., and J. Jiménez, 2009: Estimation of turbulent convection velocities and corrections to Taylor's approximation. *J. Fluid Mech.*, **640**, 5–26, https://doi.org/10.1017/S0022112009991029.

Donelan, M. A., W. M. Drennan, and K. B. Katsaros, 1997: The air–sea momentum flux in conditions of wind sea and swell.

J. Phys. Oceanogr., **27**, 2087–2099, https://doi.org/10.1175/1520-0485(1997)027<2087:TASMFI>2.0.CO;2.

Drennan, W. M., H. C. Graber, and M. A. Donelan, 1999: Evidence for the effects of swell and unsteady winds on marine wind stress. *J. Phys. Oceanogr.*, **29**, 1853–1864, https://doi.org/10.1175/1520-0485(1999)029<1853:EFTEOS>2.0.CO;2.

——, ——, D. Hauser, and C. Quentin, 2003: On the wave age dependence of wind stress over pure wind seas. *J. Geophys. Res.*, **108**, 8062, https://doi.org/10.1029/2000JC000715.

——, J. A. Zhang, J. R. French, C. McCormick, and P. G. Black, 2007: Turbulent fluxes in the hurricane boundary layer. Part II: Latent heat flux. *J. Atmos. Sci.*, **64**, 1103–1115, https://doi.org/10.1175/JAS3889.1.

Drobinski, P., P. Carlotti, R. K. Newson, R. M. Banta, R. C. Foster, and J. L. Redelsperger, 2004: The structure of the near-neutral atmospheric surface layer. *J. Atmos. Sci.*, **61**, 699–714, https://doi.org/10.1175/1520-0469(2004)061<0699:TSOTNA>2.0.CO;2.

——, ——, J. L. Redelsperger, R. M. Banta, V. Masson, and R. K. Newsom, 2007: Numerical and experimental investigation of the neutral atmospheric surface layer. *J. Atmos. Sci.*, **64**, 137–156, https://doi.org/10.1175/JAS3831.1.

Edson, J. B., and C. W. Fairall, 1998: Similarity relationships in the marine atmospheric surface layer for terms in the TKE and scalar variance budgets. *J. Atmos. Sci.*, **55**, 2311–2328, https://doi.org/10.1175/1520-0469(1998)055<2311:SRITMA>2.0.CO;2.

Fairall, C. W., and Coauthors, 2006: Turbulent bulk transfer coefficients and ozone deposition velocity in the international consortium for atmospheric research into transport and transformation. *J. Geophys. Res.*, **111**, D23S20, https://doi.org/10.1029/2006JD007597.

García-Nava, H., F. J. Ocampo-Torres, P. Osuna, and M. A. Donelan, 2009: Wind stress in the presence of swell under moderate to strong wind conditions. *J. Geophys. Res.*, **114**, C12008, https://doi.org/10.1029/2009JC005389.

Ghannam, K., G. G. Katul, E. Bou-Zeid, T. Gerken, and M. Chamecki, 2018: Scaling and similarity of the anisotropic coherent eddies in near-surface atmospheric turbulence. *J. Atmos. Sci.*, **75**, 943–964, https://doi.org/10.1175/JAS-D-17-0246.1.

Grachev, A. A., and C. W. Fairall, 2001: Upward momentum transfer in the marine boundary layer. *J. Phys. Oceanogr.*, **31**, 1698–1711, https://doi.org/10.1175/1520-0485(2001)031<1698:UMTITM>2.0.CO;2.

——, ——, J. E. Hare, J. B. Edson, and S. D. Miller, 2003: Wind stress Vector over ocean waves. *J. Phys. Oceanogr.*, **33**, 2408–2429, https://doi.org/10.1175/1520-0485(2003)033<2408:WSVOOW>2.0.CO;2.

——, and Coauthors, 2018: Air-sea/land interaction in the coastal zone. *Bound.-Layer Meteor.*, **167**, 181–210, https://doi.org/10.1007/s10546-017-0326-2.

Grare, L., L. Lenain, and W. K. Melville, 2013: Wave-coherent airflow and critical layers over ocean waves. *J. Phys. Oceanogr.*, **43**, 2156–2172, https://doi.org/10.1175/JPO-D-13-056.1.

Guala, M., S. E. Hommema, and R. J. Adrian, 2006: Large-scale and very-large-scale motions in turbulent pipe flow. *J. Fluid Mech.*, **554**, 521–542, https://doi.org/10.1017/S0022112006008871.

Hanley, K. E., and S. E. Belcher, 2008: Wave-driven wind jets in the marine atmospheric boundary layer. *J. Atmos. Sci.*, **65**, 2646–2660, https://doi.org/10.1175/2007JAS2562.1.

Hare, J. E., T. Hara, J. B. Edson, and J. M. Wilczak, 1997: A similarity analysis of the structure of airflow over surface waves. *J. Phys. Oceanogr.*, **27**, 1018–1037, https://doi.org/10.1175/1520-0485(1997)027<1018:ASAOTS>2.0.CO;2.

Högström, U., J. C. R. Hunt, and A.-S. Smedman, 2002: Theory and measurements for turbulence spectra and variances in the atmospheric neutral surface layer. *Bound.-Layer Meteor.*, **103**, 101–124, https://doi.org/10.1023/A:1014579828712.

——, E. Sahlée, A.-S. Smedman, A. Rutgersson, E. Nilsson, K. K. Kahma, and W. M. Drennan, 2015: Surface stress over the ocean in swell-dominated conditions during moderate winds. *J. Atmos. Sci.*, **72**, 4777–4795, https://doi.org/10.1175/JAS-D-15-0139.1.

——, ——, ——, ——, ——, ——, and ——, 2018: The transition from downward to upward air–sea momentum flux in swell-dominated light wind conditions. *J. Atmos. Sci.*, **75**, 2579–2588, https://doi.org/10.1175/JAS-D-17-0334.1.

Hristov, T. S., and J. Ruiz-Plancarte, 2014: Dynamic balances in a wavy boundary layer. *J. Phys. Oceanogr.*, **44**, 3185–3194, https://doi.org/10.1175/JPO-D-13-0209.1.

——, C. Friehe, and S. Miller, 1998: Wave-coherent fields in air flow over ocean waves: Identification of cooperative behavior buried in turbulence. *Phys. Rev. Lett.*, **81**, 5245–5248, https://doi.org/10.1103/PhysRevLett.81.5245.

——, S. D. Miller, and C. A. Friehe, 2003: Dynamical coupling of wind and ocean waves through wave-induced air flow. *Nature*, **422**, 55–58, https://doi.org/10.1038/nature01382.

Huang, J., and Coauthors, 2021: The turbulent structure of the marine atmospheric boundary layer during and before a cold front. *J. Atmos. Sci.*, **78**, 863–875, https://doi.org/10.1175/JAS-D-19-0314.1.

Hunt, J. C. R., and P. Carlotti, 2001: Statistical structure at the wall of the high Reynolds number turbulent boundary layer. *Flow Turbul. Combust.*, **66**, 453–475, https://doi.org/10.1023/A:1013519021030.

Hutchins, N., K. Chauhan, I. Marusic, J. Monty, and J. Klewicki, 2012: Towards reconciling the large-scale structure of turbulent boundary layers in the atmosphere and laboratory. *Bound.-Layer Meteor.*, **145**, 273–306, https://doi.org/10.1007/s10546-012-9735-4.

Kader, B. A., and A. M. Yaglom, 1991: Spectral and correlation functions of surface layer turbulence in unstable thermal stratification. *Turbulence and Coherent Structures*, O. Metais and M. Lesieur, Eds., Kluwer Academic, 388–412.

Kahma, K. K., M. A. Donelan, W. M. Drennan, and E. A. Terray, 2016: Evidence of energy and momentum flux from swell to wind. *J. Phys. Oceanogr.*, **46**, 2143–2156, https://doi.org/10.1175/JPO-D-15-0213.1.

Katul, G. G., and C. R. Chu, 1998: A theoretical and experimental investigation of energy-containing scales in the dynamic sublayer of boundary-layer flows. *Bound.-Layer Meteor.*, **86**, 279–312, https://doi.org/10.1023/A:1000657014845.

——, A. Porporato, and V. Nikora, 2012: Existence of k^{-1} power-law scaling in the equilibrium regions of wall-bounded turbulence explained by Heisenberg's eddy viscosity. *Phys. Rev. E*, **86**, 066311, https://doi.org/10.1103/PhysRevE.86.066311.

Kudryavtsev, V. N., and V. K. Makin, 2004: Impact of swell on the marine atmospheric boundary layer. *J. Phys. Oceanogr.*, **34**, 934–949, https://doi.org/10.1175/1520-0485(2004)034<0934:IOSOTM>2.0.CO;2.

Kunkel, G. J., and I. Marusic, 2006: Study of the near-wall-turbulent region of the high-Reynolds-number boundary layer using an atmospheric flow. *J. Fluid Mech.*, **548**, 375–402, https://doi.org/10.1017/S0022112005007780.

Li, Q., P. Gentine, J. P. Mellado, and K. A. McColl, 2018: Implications of nonlocal transport and conditionally averaged statistics on Monin–Obukhov similarity theory and Townsend's attached eddy hypothesis. *J. Atmos. Sci.*, **75**, 3403–3431, https://doi.org/10.1175/JAS-D-17-0301.1.

Li, S, Z. S. Zou, D. L. Zhao, and Y. J. Hou, 2020: On the wave state dependence of the sea surface roughness at moderate wind speeds under mixed wave conditions. *J. Phys. Oceanogr.*, **50**, 3295–3307, https://doi.org/10.1175/JPO-D-20-0102.1.

Mahrt, L., E. L. Andreas, J. B. Edson, D. Vickers, J. L. Sun, and E. G. Patton, 2016: Coastal zone surface stress with stable stratification. *J. Phys. Oceanogr.*, **46**, 95–105, https://doi.org/10.1175/JPO-D-15-0116.1.

Makin, V. K., and V. N. Kudryavtsev, 1999: Coupled sea surface-atmosphere model: 1. Wind over waves coupling. *J. Geophys. Res.*, **104**, 7613–7623, https://doi.org/10.1029/1999JC900006.

Marusic, I., and J. P. Monty, 2019: Attached eddy model of wall turbulence. *Annu. Rev. Fluid Mech.*, **51**, 49–74, https://doi.org/10.1146/annurev-fluid-010518-040427.

——, and A. E. Perry, 1995: A wall-wake model for the turbulence structure of boundary layers. Part 2. Further experimental support. *J. Fluid Mech.*, **298**, 389–407, https://doi.org/10.1017/S0022112095003363.

——, J. P. Monty, M. Hultmark, and A. J. Smits, 2013: On the logarithmic region in wall turbulence. *J. Fluid Mech.*, **716**, R3, https://doi.org/10.1017/jfm.2012.511.

Miles, J., 1957: On the generation of surface waves by shear flows. *J. Fluid Mech.*, **3**, 185, https://doi.org/10.1017/S0022112057000567.

Monin, A. S., and A. M. Obukhov, 1954: Basic laws of turbulent mixing in the surface layer of the atmosphere. *Tr. Geofiz. Inst. Akad. Nauk SSSR*, **24**, 163–187.

Nikora, V., 1999: Origin of the "-1" spectral law in wall-bounded turbulence. *Phys. Rev. Lett.*, **83**, 734–736, https://doi.org/10.1103/PhysRevLett.83.734.

Nilsson, E. O., A. Rutgersson, A. S. Smedman, and P. P. Sullivan, 2012: Convective boundary-layer structure in the presence of wind-following swell. *Quart. J. Roy. Meteor. Soc.*, **138**, 1476–1489, https://doi.org/10.1002/qj.1898.

Perry, A. E., and M. S. Chong, 1982: On the mechanism of wall turbulence. *J. Fluid Mech.*, **119**, 173–217, https://doi.org/10.1017/S0022112082001311.

——, and I. Marusic, 1995: A wall-wake model for the turbulence structure of boundary layers. Part 1. Extension of the attached eddy hypothesis. *J. Fluid Mech.*, **298**, 361–388, https://doi.org/10.1017/S0022112095003351.

——, S. Henbest, and M. S. Chong, 1986: A theoretical and experimental study of wall turbulence. *J. Fluid Mech.*, **165**, 163–199, https://doi.org/10.1017/S002211208600304X.

Phillips, O. M., 1977: *The Dynamics of the Upper Ocean*. 2nd ed. Cambridge University Press, 261 pp.

Rutgersson, A., A. S. Smedman, and U. Hogstrom, 2001: Use of conventional stability parameters during swell. *J. Geophys. Res.*, **106**, 27 117–27 134, https://doi.org/10.1029/2000JC000543.

Semedo, A., O. Saetra, A. Rutgersson, K. K. Kahma, and H. Pettersson, 2009: Wave-induced wind in the marine boundary layer. *J. Atmos. Sci.*, **66**, 2256–2271, https://doi.org/10.1175/2009JAS3018.1.

Smedman, A. S., X. G. Larsen, U. Hogstrom, K. K. Kahma, and H. Pettersson, 2003: Effect of sea state on the momentum exchange over the sea during neutral conditions. *J. Geophys. Res.*, **108**, 3367, https://doi.org/10.1029/2002JC001526.

——, U. Hogstrom, E. Sahlee, W. M. Drennan, K. K. Kahma, H. Pettersson, and F. Zhang, 2009: Observational study of marine atmospheric boundary layer characteristics during swell. *J. Atmos. Sci.*, **66**, 2747–2763, https://doi.org/10.1175/2009JAS2952.1.

Soloviev, Y. P., and V. N. Kudryavtsev, 2010: Wind-speed undulations over swell: Field experiment and interpretation. *Bound.-Layer Meteor.*, **136**, 341–363, https://doi.org/10.1007/s10546-010-9506-z.

Song, J., W. Fan, S. Li, and M. Zhou, 2015: Impact of surface waves on the steady near-surface wind profiles over the ocean. *Bound.-Layer Meteor.*, **155**, 111–127, https://doi.org/10.1007/s10546-014-9983-6.

Sullivan, P. P., J. B. Edson, T. Hristov, and J. C. McWilliams, 2008: Large-eddy simulations and observations of atmospheric marine boundary layers above nonequilibrium surface waves. *J. Atmos. Sci.*, **65**, 1225–1245, https://doi.org/10.1175/2007JAS2427.1.

Toffoli, A., A. Babanin, M. Onorato, and T. Waseda, 2010: Maximum steepness of oceanic waves: Field and laboratory experiments. *Geophys Res Lett*, **37**, L05603, https://doi.org/10.1029/2009GL041771.

Townsend, A. A., 1972: Flow in a deep turbulent boundary layer over a surface distorted by water waves. *J. Fluid Mech.*, **55**, 719–735, https://doi.org/10.1017/S0022112072002101.

——, 1976: *The Structure of Turbulent Shear Flow*. Vol. 2, Cambridge University Press, 450 pp.

Vickers, D., and L. Mahrt, 2003: The cospectral gap and turbulent flux calculations. *J. Atmos. Oceanic Technol.*, **20**, 660–672, https://doi.org/10.1175/1520-0426(2003)20<660:TCGATF>2.0.CO;2.

Voermans, J. J., H. Rapizo, H. Y. Ma, F. L. Qiao, and A. V. Babanin, 2019: Air–sea momentum fluxes during tropical Cyclone Olwyn. *J. Phys. Oceanogr.*, **49**, 1369–1379, https://doi.org/10.1175/JPO-D-18-0261.1.

Wang, L.-H., C.-X. Xu, H. J. Sung, and W.-X. Huang, 2021: Wall-attached structures over a traveling wavy boundary: Turbulent velocity fluctuations. *Phys. Rev. Fluids*, **6**, 034611, https://doi.org/10.1103/PhysRevFluids.6.034611.

Wu, L. C., A. Rutgersson, E. Sahlee, and X. G. Larsen, 2016: Swell impact on wind stress and atmospheric mixing in a regional coupled atmosphere-wave model. *J. Geophys. Res. Oceans*, **121**, 4633–4648, https://doi.org/10.1002/2015JC011576.

——, ——, and E. Nilsson, 2017: Atmospheric boundary layer turbulence closure scheme for wind-following swell conditions. *J. Atmos. Sci.*, **74**, 2363–2382, https://doi.org/10.1175/JAS-D-16-0308.1.

——, T. Hristov, and A. Rutgersson, 2018: Vertical profiles of wave-coherent momentum flux and velocity variances in the marine atmospheric boundary layer. *J. Phys. Oceanogr.*, **48**, 625–641, https://doi.org/10.1175/JPO-D-17-0052.1.

Yaglom, A. M., 1991: Similarity laws for wall turbulence flows. *New Approaches and Concepts in Turbulence*, T. Dracos and A. Tsinober, Eds., Birkhäuser, 7–27.

Yousefi, K., F. Veron, and M. P. Buckley, 2020: Momentum flux measurements in the airflow over wind-generated surface waves. *J. Fluid Mech.*, **895**, A15, https://doi.org/10.1017/jfm.2020.276.

Zhang, W. Y., W. X. Huang, and C. X. Xu, 2019: Very large-scale motions in turbulent flows over streamwise traveling wavy boundaries. *Phys. Rev. Fluids*, **4**, 054601, https://doi.org/10.1103/PhysRevFluids.4.054601.

Zou, Z. S., D. L. Zhao, B. Liu, J. A. Zhang, and J. Huang, 2017: Observation-based parameterization of air-sea fluxes in terms of wind speed and atmospheric stability under low-to-

moderate wind conditions. *J. Geophys. Res. Oceans*, **122**, 4123–4142, https://doi.org/10.1002/2016JC012399.

——, J. B. Song, P. L. Li, J. Huang, J. A. Zhang, Z. H. Wan, and S. Q. Li, 2019: Effects of swell waves on atmospheric boundary layer turbulence: A low wind field study. *J. Geophys. Res. Oceans*, **124**, 5671–5685, https://doi.org/10.1029/2019JC015153.

——, S. Q. Li, J. Huang, P. L. Li, J. B. Song, J. A. Zhang, and Z. H. Wan, 2020: Atmospheric boundary layer turbulence in the presence of swell: Turbulent kinetic energy budget, Monin–Obukhov similarity theory, and inertial dissipation method. *J. Phys. Oceanogr.*, **50**, 1213–1225, https://doi.org/10.1175/JPO-D-19-0136.1.